Journal of Nuclear Materials 400 (2010) 218–231

Contents lists available at ScienceDirect

Journal of Nuclear Materials

journal homepage: www.elsevier.com/locate/jnucmat

On the potential of tungsten–vanadium composites for high temperature application with wide-range thermal operation window

Jörg Hohe [a,*], Peter Gumbsch [b]

[a] Fraunhofer Institut für Werkstoffmechanik Wöhlerstr. 11, 79108 Freiburg, Germany
[b] Universität Karlsruhe, Institut für Zuverlässigkeit von Bauteilen und Systemen Kaiserstr. 12, 76131 Karlsruhe, Germany

ARTICLE INFO

Article history:
Received 2 December 2009
Accepted 15 March 2010

ABSTRACT

The present study is concerned with the numerical design of a composite material consisting of tungsten and vanadium for application in future nuclear fusion plants. The proposed composite material combines a significant creep resistance at high temperatures with a reasonable fracture toughness in the low temperature range and, compared to its constituents, features an enhanced thermal operation window. In a first step, a numerical screening analysis is performed for a comparison of different types of composite materials including particle, short fiber and infinite fiber reinforced composites with both, regular and random microstructures. The different options are compared with respect to their thermal and mechanical properties as well as their creep resistance. In a preliminary experimental investigation, a first trial heat of the composite is processed and tested for its creep resistance at 1000 °C and its fracture toughness at ambient temperature. The results reveal a distinct potential of the material.

1. Introduction

The choice of materials for high temperature application in nuclear fusion reactors is a challenging task, especially for the plasma facing components in the first wall and divertor regions, since rather different and in some cases contradictory requirements have to be satisfied. In this context, gas cooled divertor concepts, as they have been extensively studied in the recent time, require an operation temperature of 1200–1300 °C at the upper end. Considerably high admissible stress limits are mandatory due to the loads resulting from high-pressure Helium cooling. In addition to a considerable stress carrying capacity at high temperatures, a sufficiently large toughness is required at lower temperatures ranging from 800 °C down to ambient temperature in order to prevent brittle failure of the material in areas at lower temperatures and during plant start-up or shut-down.

Beyond the pure mechanical requirements, an excellent thermal conductivity is mandatory for materials to be used in first wall and divertor applications in order to keep the temperature and the secondary stresses resulting from temperature gradients and constrained thermal strains within acceptable limits. For the same reason, a low coefficient of thermal expansion is required. Furthermore, materials used in a nuclear fusion environment must not feature distinct embrittlement and damage effects due to neutron irradiation. For reasons of nuclear waste management, low activation properties and rapid decay of the radiation in the case of activated materials are mandatory to ensure that the waste properties at the end-of-life of the respective components are within acceptable limits. Hydrogen compatibility is mandatory due to the exposure of first wall and divertor components to hydrogen isotopes such as tritium. With regard to the long-term availability of nuclear fusion power plants, an excellent erosion resistance of all plasma facing materials is mandatory. Finally, limits are set by the availability of some of the potential candidate materials.

Due to these ambitious and partially contradictory requirements, only few materials can be used in first wall and especially divertor applications, as it has been pointed out, among others, by Tavassoli [25] as well as Zinkle and Ghoniem [29]. All of the candidate materials, especially those with good high temperature applicability suffer from a restricted thermal operation window (Fig. 1), even when possible extensions into the sub-optimal ranges as marked in light grey in Fig. 1 are considered. The upper end of the thermal operation window for refractory alloys is defined by the re-crystallization temperature associated with a rapidly decreasing creep resistance. Corrosion and helium embrittlement set further limits. The lower end of the thermal operation window is defined by the ductile-to-brittle transition, below which an inherent brittle material behaviour with rather low fracture toughness is obtained. Especially at the lower bound, the width of the thermal operation window may be further reduced by irradiation damage effects resulting in an embrittlement of the material with increasing ductile-to-brittle transition temperature.

Among all possible materials, tungsten is the primary material candidate for plasma facing components since it features the highest melting temperature of all metals, together with a superior

* Corresponding author. Tel.: +49 761 5142 340; fax: +49 761 5142 401.
E-mail address: hohe@iwm.fhg.de (J. Hohe).

0022-3115/$ - see front matter © 2010 Elsevier B.V. All rights reserved.
doi:10.1016/j.jnucmat.2010.03.007

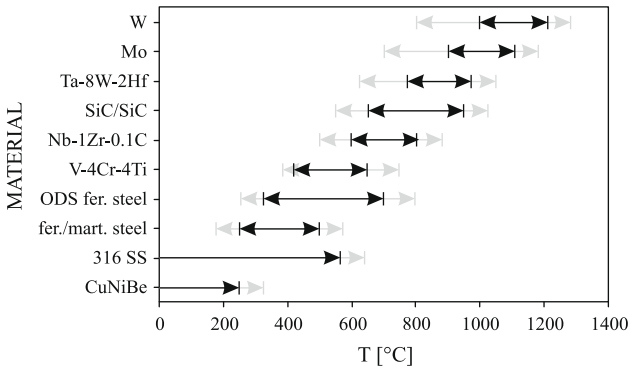

Fig. 1. Thermal application windows for fusion materials (re-drawn from results presented by Zinkle and Ghoniem [29]).

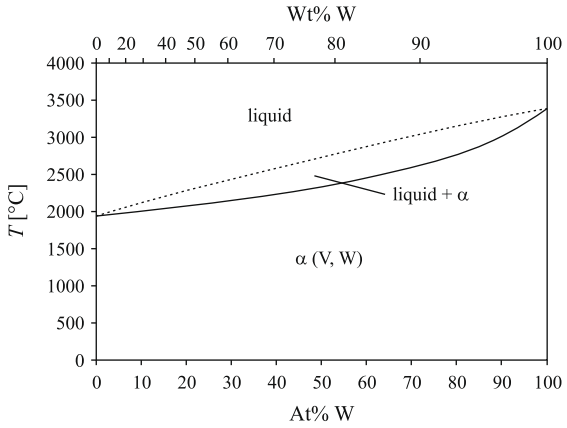

Fig. 2. W–V-phase diagram (re-drawn from Brandes and Brooke [5]).

thermal conductivity, low activation under neutron irradiation and good erosion resistance. Nevertheless, tungsten suffers from a rather low fracture toughness at low temperatures which additionally features a strong dependence on the crack orientation within the crystal lattice [10,11,17,21]. Fracture toughness values reported in the literature for ambient temperature range from lows of approximately 2 $MPam^{1/2}$ obtained by Dümmer et al. [8] in compressive tests on polycrystalline tungsten for small cracks to a range from 6 $MPam^{1/2}$ up to an extreme value of 20 $MPam^{1/2}$ (depending on the crack orientation) obtained for tungsten single crystals [11,21]. To enhance the thermal operation window of tungsten, different tungsten alloys such as W–26Re, W–1La_2O_3, K-doped tungsten or W–Ni–Fe-alloys (e.g. [19,20]) have been investigated. Nevertheless, most of these materials are inherently brittle at ambient temperature. Although a considerable increase in the fracture toughness beyond 400 °C is reported by Mutoh et al. [18] for a tungsten–rhenium alloy, even for this material only slight enhancements are observed below this temperature. Possible enhancements in the fracture toughness of tungsten by alloying with other metals in most cases result in a loss of the high-temperature capability of tungsten towards the upper end of the thermal operation window.

As an alternative to the use of tungsten, there is a strong trend towards the use of vanadium alloys, especially V–4Cr–4Ti, with an enhanced creep resistance at the upper end of the thermal operation window (e.g. [6,16]). A broad review of the potential of this material with regard to its thermomechanical properties, design limits as well as irradiation and environmental aspects has been provided by Kurtz et al. [15]. Environmental aspects are also studied by Li et al. [16]. Nevertheless, although this material does not feature the excessive creep of pure vanadium [28] towards the upper end of the necessary design window, its creep resistance at higher temperatures is still insufficient.

A possibility to circumvent the problem that materials with good toughness at low temperatures feature a poor high-temperature creep resistance whereas creep resistant materials in general feature an inherently brittle behaviour at low temperature might be the design of metal–metal composites. However, materials of this type have not been studied systematically in the past. Rare exceptions are the studies by Vill et al. [26] on molybdenum toughened tungsten microlaminates. A problem for manufacture of this material system – which in a similar manner also occurs for the tungsten–vanadium composites proposed in the present study – is the formation of solid solutions of the two metals with no reported intermediate phases as it can be observed in the phase diagram for the tungsten–vanadium system in Fig. 2 [5]. A possibility to circumvent this problem might be the reduction in processing time in order to reduce the available time for diffusion processes. A general problem for employing vanadium or its alloys derives from the problem of sputtering and the resulting plasma contamination. On the other hand, a tungsten armor of the vanadium components or – especially when using metal–metal composites – the design of a functionally graded material with an increasing tungsten content towards the plasma facing surface might resolve this problem.

The objective of the present study is an exploration of the potential of tungsten–vanadium composites with respect to their potential for application in plasma facing components. In a first stage of the study, a numerical screening analysis is performed, where the effective thermomechanical material response of different options for the design of composite materials is determined by a numerical homogenization analysis. Four different types of composites are studied including particle reinforced materials, short fiber reinforced materials with both randomly oriented and aligned fibers as well as unidirectionally infinite fiber reinforced materials. In most cases, the vanadium phase is assumed to form the matrix. In all cases, the inclusion volume fraction is varied over the range from approximately 10% up to 50%. The different options are compared with respect to their thermal conductivity, their thermal expansion, their elastic constants and their yield curves throughout the temperature range from ambient temperature up to 1200 °C. In addition, their creep resistance at high temperatures and their possible fracture toughness enhancement at low temperatures are analyzed. In a second stage, a trial heat of the material is processed and tested for its creep resistance at a temperature of 1000 °C as well as for its fracture toughness at ambient temperature.

2. Numerical homogenization

2.1. General concept

In a first approach, a numerical screening analysis of different options for the design of the microstructure of the proposed tungsten–vanadium composite is performed. For this purpose, the macroscopic "effective" thermomechanical properties of the different composite options are computed numerically by means of an energy-based homogenization technique [3]. In the special form utilized here, the technique has originally been developed for the analysis of the effective mechanical material response of cellular solids [13,14].

Mathematically, the general mechanical homogenization problem can be defined as follows: Consider a body Ω according to Fig. 3, consisting of any type of microstructured composite material. The body Ω is bounded by an external boundary $\partial\Omega = \partial\Omega^t \cup \partial\Omega^u$. On $\partial\Omega^t$, the components $t_i = \sigma_{ij} n_j$ of the traction vector

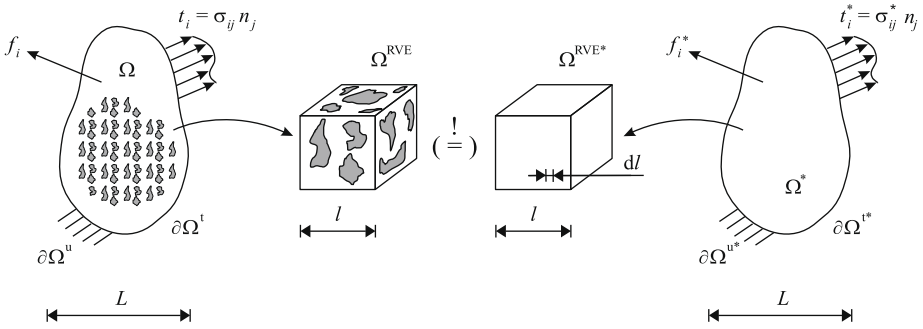

Fig. 3. Concept of the representative volume element.

are prescribed, where σ_{ij} are the components of the (Cauchy-) stress tensor and n_j are the components of the outward normal unit vector. On $\partial\Omega^u$, the components u_i of the displacement vector are prescribed. In addition to the boundary loads t_i and u_i, the body Ω might be subjected to distributed loads f_i.

For reasons of computational efficiency, the body Ω is replaced by a similar body Ω^* with identical size and external shape. The substitute body Ω^* is assumed to consist of a (quasi-) homogeneous, "effective" material with yet unknown properties. The properties of the effective material have to be chosen such that the mechanical response of the bodies Ω and Ω^* is equivalent on the macroscopic level of structural hierarchy, provided that both bodies are subject to macroscopically equivalent external loads. For determination of the effective material properties, a representative volume element Ω^{RVE} for the microstructure is considered. For periodic microstructures, the representative volume element can be chosen as the smallest repeating microstructural assembly. For nonperiodic microstructures, the representative volume element has to be statistically representative or, alternatively, the nonperiodic microstructure is idealized by a periodic assembly. In all cases, the characteristic length l of the volume element is much smaller than the characteristic length L of the entire body Ω, but not infinitesimally small ($L \gg l \gg \mathrm{d}l$, see Fig. 3). The effective material properties have to be chosen such that the mechanical response of Ω^{RVE} and a similar volume element Ω^{RVE*} consisting of the effective medium is equivalent on this intermediate, "mesoscopic" level of structural hierarchy.

Within the strain energy-based homogenization concept, mesoscopic mechanical equivalence is defined by the condition that the average strain energy density

$$\bar{w} = \frac{1}{V^{RVE}} \int_{\Omega^{RVE}} w\,\mathrm{d}V = \frac{1}{V^{RVE*}} \int_{\Omega^{RVE*}} w^*\,\mathrm{d}V = \bar{w}^* \tag{1}$$

in both volume elements is equal, provided that both volume elements are subject to an equivalent state of deformation defined by the condition that the volume average

$$\bar{\varepsilon}_{ij} = \frac{1}{V^{RVE}} \int_{\Omega^{RVE}} \varepsilon_{ij}\,\mathrm{d}V = \frac{1}{V^{RVE*}} \int_{\Omega^{RVEast}} \varepsilon_{ij}^*\,\mathrm{d}V = \bar{\varepsilon}_{ij}^* \tag{2}$$

of the deformation gradient F_{ij} for both volume elements is equal. The effective stress and strain components $\bar{\sigma}_{ij}^*$ and $\bar{\varepsilon}_{ij}^*$ are determined from the effective strain energy density $\bar{w}$ and the effective deformation gradient $\bar{F}_{ij}$ using their standard definitions on the mesoscopic level [13,14].

The mechanical homogenization concept (1) and (2) can be extended to thermal problems in a straight forward manner. In this context, the mesoscopic thermal equivalence of both volume elements is defined by the condition that the average heat flux density

$$\bar{\dot{q}}_i = \frac{1}{V^{RVE}} \int_{\Omega^{RVE}} \dot{q}_i\,\mathrm{d}V = \frac{1}{V^{RVE*}} \int_{\Omega^{RVE*}} \dot{q}_i^*\,\mathrm{d}V = \bar{\dot{q}}_i^* \tag{3}$$

in both elements has to be equal, provided that both volume elements are subject to a temperature gradient

$$\overline{T}_{,i} = \frac{1}{V^{RVE}} \int_{\Omega^{RVE}} T_{,i}\,\mathrm{d}V = \frac{1}{V^{RVE*}} \int_{\Omega^{RVE*}} T_{,i}^*\,\mathrm{d}V = \overline{T}_{,i}^* \tag{4}$$

which is equal in an integral average sense.

2.2. Numerical implementation

The application of the energy-based homogenization procedure defined by Eqs. (1)–(4) requires that a numerical model for of the representative volume element has to be subjected to one or more reference strain states or reference temperature gradients. For each of the reference states, the effective strain energy density or the effective heat flux density is computed by means of the finite element method. Subsequently, the effective properties are determined from the relations between the energetic quantities $\bar{w}$ and $\bar{\dot{q}}$ on one hand and the corresponding kinematic quantities $\bar{\varepsilon}_{ij}$ and $\overline{T}_{,i}$ on the other hand. The reference states for the effective strains $\bar{\varepsilon}_{ij}$ and the effective thermal gradients $\overline{T}_{,i}$ are assumed to be distributed homogeneously on the macroscopic level. In this case, due to the geometric periodicity of the microstructure, the microscopic (local) states of deformation F_{ij} and the microscopic temperature gradients $T_{,i}$ have to be periodic. Hence, periodic boundary conditions apply to the representative volume element, requiring a similar deformation and temperature gradient at all corresponding points on opposite RVE surfaces (see Fig. 4).

Subsequently, the discrete boundary conditions for each pair of corresponding nodes on the external RVE surfaces are obtained by transforming the volume integrals in the kinematic equivalence

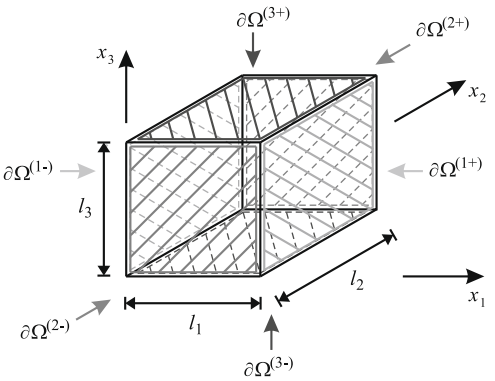

Fig. 4. Boundary conditions.

conditions (2) and (4) into boundary integrals using Green's theorem, substituting the periodic boundary conditions into the results and evaluating the remaining integrals [13,14]. For a brick-shaped representative volume element with the edge lengths l_1, l_2 and l_3 as shown in Fig. 4, the discrete boundary conditions read

$$\frac{u_i^{(j+)} - u_i^{(j-)}}{l_{(j)}} = \overline{F}_{ij} - \delta_{ij} \tag{5}$$

$$\frac{T^{(j+)} - T^{(j-)}}{l_{(j)}} = \overline{T}_{,j} \tag{6}$$

where no summation is to be performed with respect to the indices in parentheses. Four additional boundary conditions are required to prevent translatoric rigid body motions and temperature shifts of the representative volume element.

In the numerical implementation, Eqs. (5) and (6) are introduced directly as additional constraint equations into the nonlinear system of equations set up by the finite element discretization of the representative volume element. Hence, the effective deformation and temperature gradients $\bar{\varepsilon}_{ij}$ and $\overline{T}_{,i}$ are introduced as generalized degrees of freedom so that the corresponding effective stress and heat flux components are obtained directly from the finite element solution, since they are the energetic conjugates to the effective strains and temperature gradients. Therefore, using Eqs. (5) and (6) as additional equations within the system of equations of the regular finite element method, the energetic homogenization scheme defined by Eqs. (1)–(4) can be used in a numerically rather efficient manner with no need to evaluate the respective volume integrals.

3. Microstructural design options and constituent material properties

In the numerical screening analysis, four different types of composite microstructure are investigated:

- *Particle* reinforced composites: random distribution of spherical particles with equal size embedded into a homogeneous matrix.
- *Randomly* oriented short fiber reinforced composites: randomly oriented and randomly distributed ellipsoidal particles with an aspect ratio of 1:5 embedded into a homogeneous matrix.
- *Aligned* short fiber reinforced composites: aligned but randomly distributed ellipsoidal particles with an aspect ratio of 1:5 embedded into a homogeneous matrix.
- *Unidirectionally* (UD) infinite fiber reinforced composites: aligned (quasi-) infinite fibers with circular cross section embedded into a homogeneous matrix.

The particle reinforced composites might be manufactured using powder metallurgical routes where either tungsten or vanadium might form the matrix phase. The fibrous composite types might be produced by embedding tungsten wire into a powder metallurgically produced vanadium matrix. Therefore, vanadium is assumed to form the matrix material in all cases, except for the particle composite, where both vanadium and tungsten matrices are investigated. Three different inclusion volume fractions (approximately 50%, 30% and 10%) are investigated for each type of composite material.

In all cases unit cells with periodic microstructure are used as representative volume elements. The position and – in case of the random short fiber reinforced composite type – the spatial orientation of the inclusions within the representative volume elements are determined randomly using a random number generator. For the unidirectionally infinite fiber reinforced composite, the fiber orientation is prescribed, whereas for the aligned short fiber reinforced type, initially randomly oriented fibers are re-positioned and re-oriented by means of a "shaking" algorithm. The models for the particle and short fiber composites are meshed by standard displacement based four-node tetrahedral finite elements whereas eight-node brick elements are employed in the models of the UD fiber composites due to the easier mesh construction by extrusion of a two-dimensional auxiliary mesh. The composite materials are assumed to be initially stress free at a temperature of $T = 1200\,^{\circ}\mathrm{C}$.

The microstructural models for all composite types contain exactly three complete inclusions (which may be divided into parts

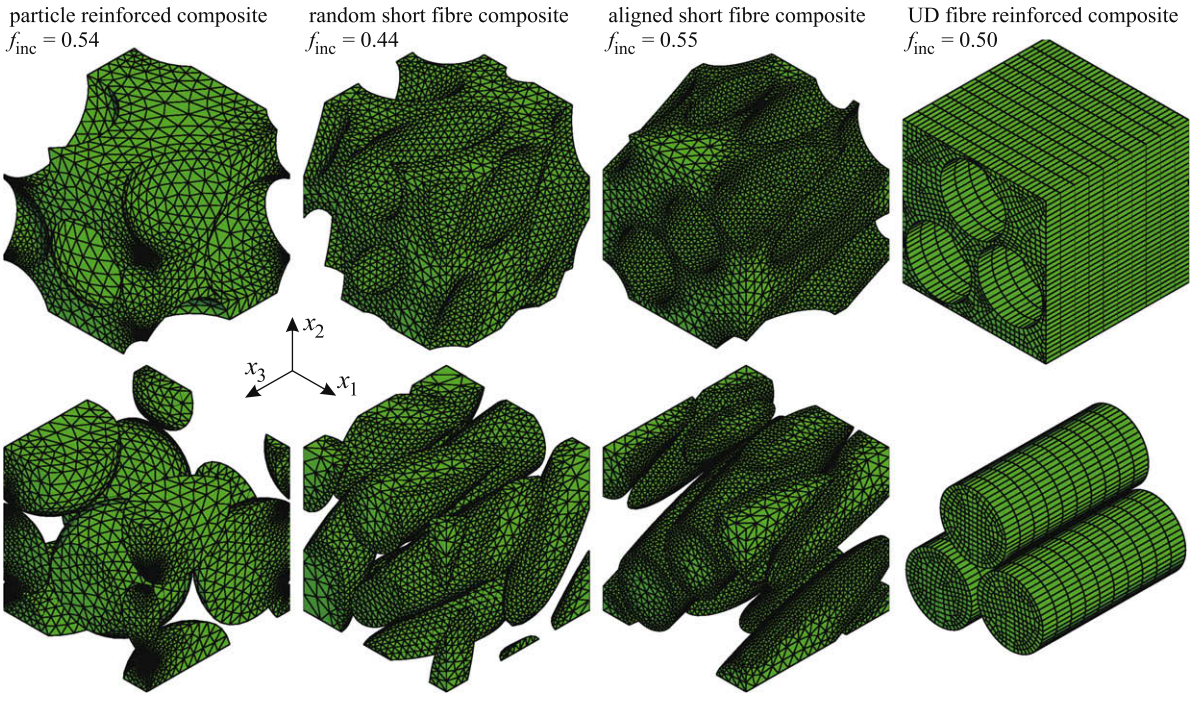

Fig. 5. Finite element models for considered microstructural design options (matrix and inclusions separated).

by the external surfaces of the volume elements). Although the microstructural disorder implies a variety of possible microstructural geometries, a single finite element model per composite type is considered, except for the random short fiber reinforced composite with approximately 30% inclusion volume fraction, where three different microstructures are investigated in order to assess possible scatter effects due to geometric material inhomogeneity in some more depth. In all other cases, the effect of the randomness is accounted for by all possible applied loading directions for each considered load case. Examples for the finite element models of the different types of composite microstructures at approximately 50% inclusion volume fraction are presented in Fig. 5.

The mechanical material behaviour of the two constituent phases is assumed to be linear elastic governed by the elastic constants E and ν, followed by work hardening plastic range described by standard J_2-plasticity with a linear or bi-linear yield curve $\sigma_y\left(\varepsilon_e^{pl}\right)$. The heat conduction is described by a linear heat conduction law with the thermal conductivity λ. The thermal expansion for the constituent phases is assumed to be governed by α^{th} as the temperature-dependent coefficient of thermal expansion. The (secondary) creep at elevated temperatures is modeled by Norton's creep law with scaling constant A and exponent n. The material properties are collected from different literature sources [4,5,20,24,25,27–29]. The data used in the numerical analyses are compiled in Tables 1 and 2. Between the discrete values, the material parameters are interpolated in a linear manner. Outside the presented ranges, the properties are assumed to be constant. It has to be mentioned that the properties strongly depend on the manufacturing and heat treatment process. Therefore, distinct differences between the parameters occur in different literature sources, and great care has to be taken when using the parameters given in Tables 1 and 2.

4. Numerical results

4.1. Thermal conductivity

The first effective property considered in the numerical screening analysis regarding the potential of the different microstructural design options is the effective thermal conductivity $\bar{\lambda}$. For plasma facing application, an excellent thermal conductivity is essential in order to enable efficient cooling to keep the material temperature within acceptable limits even though the external medium temperature by far exceeds these limits.

For determination of the effective thermal conductivity $\bar{\lambda}$, the representative volume elements are loaded by effective temperature gradients of $\overline{T}_{,i} = 10\,\mathrm{K/mm}$ for which the effective heat flux density $\bar{\dot{q}}_i$ through the cross section of the representative volume element is computed. In order to account for spatial orientation effects, the prescribed effective temperature gradient is applied with respect to all three principal spatial directions (x_1-, x_2- and x_3-directions) in separate analyses. For the case of the short fiber reinforced composite with aligned fibers, where the fiber direction does not coincide with either of these direction, a transformation into an auxiliary system is performed, where one of the axes is oriented towards the fiber direction. From the results, the effective thermal conductivity

$$\bar{\lambda}_i = -\frac{\bar{\dot{q}}_{(i)}}{\overline{T}_{,(i)}} \tag{7}$$

Table 1
Material parameters assumed for vanadium in the numerical screening analysis.

T [°C]	λ [W/mK]	α^{th} [10^{-6}/s]	E [GPa]	ν [–]	$\sigma_y(0)$ [MPa]	$\sigma_y(0.1)$ [MPa]	$\sigma_y(0.25)$ [MPa]	A [MPa^{-n}/s]	n [–]
20		9.1		0.35	360		430	1.000×10^{-28}	1.0000
200	31.0				270		360		
300	30.7	10.0	125						
400	31.3	10.3	124						
500		10.7	123						
550								1.000×10^{-28}	1.0000
600	33.3	11.0	122					1.139×10^{-24}	6.3370
650								1.139×10^{-24}	6.3370
700		11.4	121					1.268×10^{-20}	5.0249
725								5.771×10^{-18}	4.1342
800	36.0				245		360	3.654×10^{-14}	2.8875
900								3.654×10^{-14}	2.8875
1000	36.0								
1200	42.4				105		154	5.063×10^{-10}	4.8654

Table 2
Material parameters assumed for tungsten in the numerical screening analysis.

T [°C]	λ [W/mK]	α^{th} [10^{-6}/s]	E [GPa]	ν [–]	$\sigma_y(0)$ [MPa]	$\sigma_y(0.1)$ [MPa]	$\sigma_y(0.25)$ [MPa]	A [MPa^{-n}/s]	n [–]
20	167	4.5	400	0.280	827	1235	1235	1.0×10^{-28}	1.0
100	159	4.5			667	1017	1017		
200					579	920	920		
300					477	813	813		
400					477	754	754		
500	121	4.6	390	0.285	477	725	725		
600					477	798	798		
700					428	637	637		
800					360	453	453		
1000	111	4.6	370	0.290					
1150								1.0×10^{-28}	1.0
1200	107	4.8	354	0.292	296	370	370	2.3×10^{-13}	3.0

for the respective loading direction x_i is computed. In Eq. (7), the indices in parentheses on the right-hand side indicate that no summation is performed with respect to the repeated indices i. The analyses are performed for temperatures of 20 °C, 600 °C and 1200 °C, covering the entire range from ambient temperature to the upper end of the intended thermal operation window. The results for the different temperatures are presented in Fig. 6a–c as a function of the tungsten volume fraction f_W. For information, the thermal conductivities assumed for pure tungsten and pure vanadium are included into this as well as all subsequent figures.

For the particle reinforced composites with both vanadium and tungsten matrices as well as for the short fiber reinforced composite with random fiber orientation, the tungsten volume fraction f_W is found to be the most important parameter. All results obtained for these composite types at similar tungsten volume fractions f_W are found close together featuring only slight variations for different thermal loading directions. Slightly higher effective thermally conductivities $\bar{\lambda}$ are obtained for the vanadium particle toughened tungsten matrix composite compared to the vanadium matrix types due to the missing necessity of heat transmission through the vanadium phase with its lower local conductivity.

Although the tungsten volume fraction f_W proves to be the most important constituent parameter for the effective thermal conductivity $\bar{\lambda}$, the results for all cases of composites with random microstructure are overestimated by the rules of mixture which predict the effective thermal conductivity by a simple linear scaling law from the volume fractions f_W and f_V of the constituent materials. Only for the infinite unidirectionally fiber reinforced composites and, with some minor drawbacks, for the aligned short fiber reinforced composites, the simple scaling law provides reliable predictions, provided that the direction of the thermal gradient coincides with the tungsten fiber direction. Due to the alignment of the inclusions, the unidirectionally and the aligned short fiber composite feature a systematic anisotropy of their effective thermomechanical properties. Hence, although they feature improved properties within the fiber direction, the aligned fiber composites are outperformed by their random counterparts for thermal gradients perpendicular to the tungsten fiber direction.

From the results presented in Fig. 6a–c, no specific composite type is clearly preferred. With respect to a material design for optimum thermal conductivity, irrespective of the microstructural design, a material with a high tungsten volume fraction is desirable.

4.2. Thermal expansion

The second important effective material property related to thermal features is the effective coefficient of thermal expansion. For plasma facing components, as well as for all other components subjected to severe temperature gradients, a low thermal expansion is required in order to keep the thermally induced (secondary) stresses caused by constrained thermal expansion within acceptable limits.

The effective coefficients of thermal expansion are determined from analyses, where a homogeneously distributed temperature T is applied to the representative volume elements. No mechanical loads $\bar{\sigma}_{ij}$ or deformations $\bar{F}_{ij}$ are applied. The temperature T is varied stepwise from ambient temperature up to $T = 1200$ °C. In order to account for internal deformation constraints and residual stresses caused by the thermal mismatch of the two constituents, the material is assumed to be initially stress free at $T = 1200$ °C. A cooling and re-heating cycle starting at this temperature (cooling to ambient temperature and a subsequent re-heating to the desired temperature) is applied to these as well as to all subsequent thermo-mechanical analyses. From the resulting effective normal strains $\bar{\varepsilon}_{ij}$ determined from $\bar{F}_{ij}$, the effective coefficients of thermal expansion

$$\bar{\alpha}_i^{\mathrm{th}}(T) = \frac{\bar{\varepsilon}_{(ii)}(T) - \bar{\varepsilon}_{(ii)}(20\,^{\circ}\mathrm{C})}{T - 20\,^{\circ}\mathrm{C}} \tag{8}$$

are computed. Again, the indices in parentheses indicate that Einstein's convention does not apply. Notice that due to the microstructure of the composite materials, their effective thermal expansion might be anisotropic.

The results are presented in Fig. 7a–c. Again, the individual results $\bar{\alpha}_i^{\mathrm{th}}$ are related to the directions x_i of the global system except for the short fiber reinforced composite with aligned fibers, where a fiber orientation-related auxiliary system is used. Despite some minor scatter, the results for all composite types with random microstructures are found close to the prediction obtained by the rules of mixture. A tendency of the results towards the coefficient of thermal expansion for pure tungsten is caused by the larger stiffness of the tungsten phase compared to the vanadium phase. For both tungsten fiber composites with a preferred fiber orientation, UD infinite fiber and aligned short fiber composites, distinct differences are observed between the thermal expansion parallel and perpendicular to the fiber directions. Parallel to the fiber direction, a smaller thermal expansion and thus an effective behaviour closer to the behaviour of pure tungsten are obtained. Perpendicular to the fiber direction, the rules of mixture provide a reasonable approximation. For the objective of a small thermal expansion, a high tungsten volume fraction is preferred.

4.3. Elastic properties

For an assessment of the static mechanical material response, the effective elastic constants as well as the effective yield curves are required. The mechanical material response is determined from analyses where – in a first step – the representative volume ele-

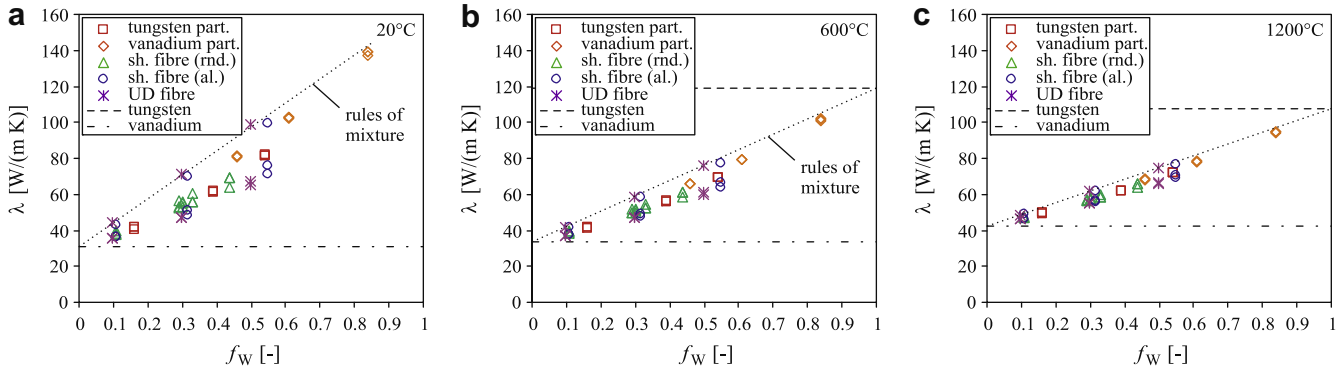

Fig. 6. Effective thermal conductivity at different temperatures.

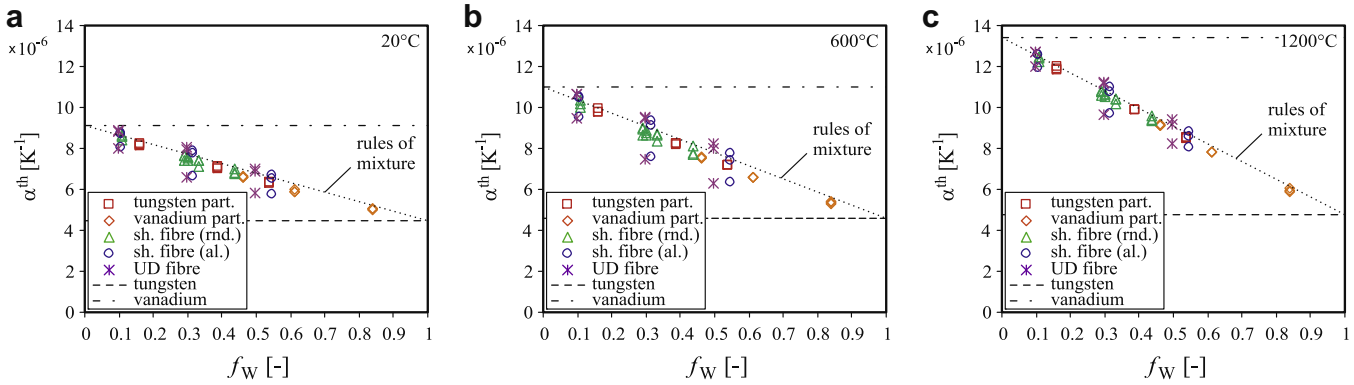

Fig. 7. Effective coefficient of thermal expansion at different temperatures.

ment is cooled down from $T = 1200\,^{\circ}C$ to ambient temperature and re-heated to the desired temperature. As for the determination of the effective thermal expansion, the initial thermal load cycle without mechanical loads or restraints is necessary to account for the residual stress state due to the thermal mismatch of the two phases and a possible local plastic deformation during cooling down from processing temperature. This type of modelling provides the most severe manner of accounting for the effects of residual stresses. In reality, the developing residual stresses might be slightly lower due to creep effects during the initial part of the cooling cycle at elevated temperatures and some possible micro damage. Nevertheless, the modelling of the thermally induced residual stresses in the most severe manner provides an improved opportunities for assessment of their effects.

In a second step of the numerical analysis, the representative volume elements are deformed in effective uniaxial stress states, where one of the effective normal or shear strain components $\bar{\varepsilon}_{ij}$ is prescribed whereas all remaining effective strain components are left unconstrained. The prescribed strain component is increased stepwise up to a nominal strain of $\bar{\varepsilon}_{ij} = 0.25$. The remaining effective strain components and the corresponding effective stresses are computed.

Under the assumption of orthotropic elasticity, the effective Young's moduli and Poisson's ratios

$$\bar{E}_i = \frac{\bar{\sigma}_{(ii)}}{\bar{\varepsilon}^{el}_{(ii)}} \tag{9}$$

$$\bar{\nu}_{ij} = -\frac{\bar{\varepsilon}^{el}_{(jj)}}{\bar{\varepsilon}^{el}_{(ii)}} \tag{10}$$

are determined. The elastic strains are determined as the differences

$$\bar{\varepsilon}^{el}_{ij} = \bar{\varepsilon}^{tot}_{ij} - \bar{\varepsilon}^{pl}_{ij} \tag{11}$$

between the effective total strains $\bar{\varepsilon}^{tot}_{ij}$ and the effective plastic strains $\bar{\varepsilon}^{pl}_{ij}$ obtained as the volume averages of the local plastic strains. Notice that both elastic constants are subject to minor changes during the loading history due to local plastic deformation.

In Fig. 8a–c, the effective Young's moduli at the onset of an overall plastic deformation of the representative volume elements are presented. In general, the tungsten volume fraction f_W has again the largest influence on the effective elastic modulus. As expected, all results for random microstructures are found close to the prediction by the rules of mixture, with a distinct tendency towards the respective value for pure vanadium as the less stiff phase.

For the aligned fiber reinforced composites (UD and aligned short fiber types), distinct differences between the fiber direction and the perpendicular directions are obtained due to their systematic anisotropy. Especially at ambient temperature, the effective Young's modulus parallel to the fiber direction is much larger than predicted by the rules of mixture. This unusual effect is caused by the internal straining of the composites during the thermal loading cycle. Since the tungsten phase has the smaller coefficient of thermal expansion, the tungsten fibers are subject to compressive deformation and thus compressive residual stresses after cooling down from the stress-free temperature. The vanadium matrix is subject to tensile residual stresses which may locally exceed the yield stress. Hence, the deviatoric part of the tensile stresses is partially relieved by plastic deformation. Nevertheless, the volumetric part of the residual stresses does not decline and may even increase due to a stress redistribution during local (microscopic) plastic deformation. As a result, a highly constrained microstructure develops, featuring a much stiffer behaviour than expected.

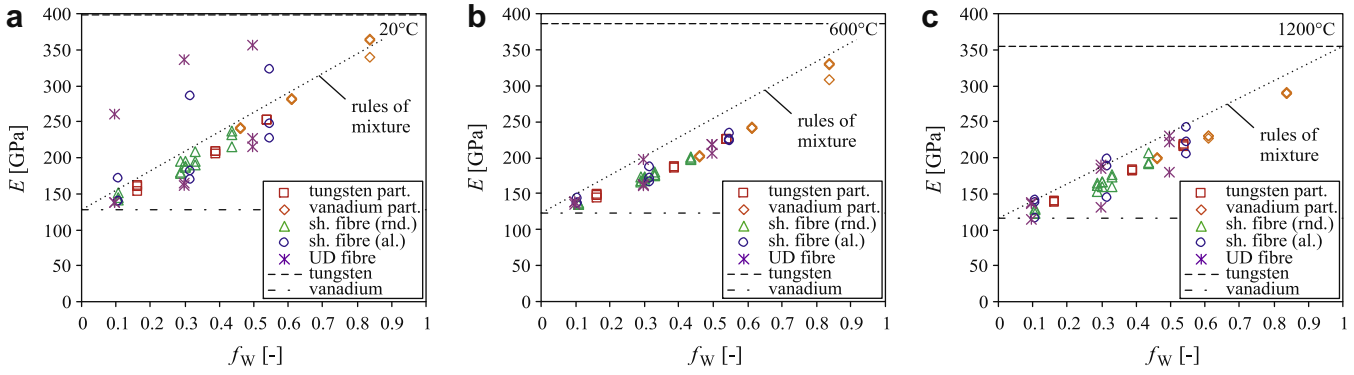

Fig. 8. Effective Young's modulus at different temperatures.

If the microstructures are re-heated, the thermally induced deformation and the related stresses decrease as it is observed in Fig. 8b. Hence, less distinct and finally vanishing effects on the effective Young's moduli $\bar{E}$ are obtained. At a temperature of 1200 °C, the opposite effect on the effective stiffness is obtained. Due to plastic deformation during cooling, the composite is no longer stress free at this temperature. Instead, a low residual stress state, although not entirely residual stress free, is obtained at an intermediate temperature level.

Another effect of the thermally induced residual stresses in conjunction with a local plastic deformation is the feature that the Young's moduli for pure vanadium and pure tungsten do not form rigorous mathematical bounds on the effective Young's moduli of the composite material as they would do in the case of a microstructure free of residual stresses [12]. For the effective Poisson's ratio $\bar{\nu}$, the respective parameters of the constituents do not provide bounds on the effective parameters of composite materials [12] since the effective Poisson's ratio is governed by the mechanisms of microstructural deformation. Consequently, a distinct scatter of the effective Poisson's ratios is observed in Fig. 9a–c. The majority of the results are found in the range between 0.3 and 0.45 for ambient temperature with a tendency towards smaller values with increasing temperature.

4.4. Yield curves

The effective yield curves $\bar{\sigma}_e(\bar{\varepsilon}_e)$ are determined from all six basic load cases (uniaxial and pure shear stress states) mentioned in Section 4.3 using the definitions

$$\bar{\sigma}_e = \left(\frac{3}{2}\bar{\sigma}'_{ij}\bar{\sigma}'_{ij}\right)^{\frac{1}{2}} \quad \text{where} \quad \bar{\sigma}'_{ij} = \bar{\sigma}_{ij} - \frac{1}{3}\bar{\sigma}_{kk}\delta_{ij} \tag{12}$$

and

$$\bar{\varepsilon}^{pl}_e = \int_0^{\bar{\varepsilon}_{ij}} \left(\frac{2}{3}\mathrm{d}\bar{\varepsilon}^{pl'}_{ij}\,\mathrm{d}\bar{\varepsilon}^{pl'}_{ij}\right)^{\frac{1}{2}} \quad \text{where} \quad \mathrm{d}\bar{\varepsilon}^{pl'}_{ij} = \mathrm{d}\bar{\varepsilon}^{pl}_{ij} \tag{13}$$

of the v.Mises equivalent stress $\bar{\sigma}_e$ and the accumulated equivalent plastic strain $\bar{\varepsilon}^{pl}_e$ in dependence on the effective stress and strain components $\bar{\sigma}_{ij}$ and $\bar{\varepsilon}^{pl}_{ij}$. In Fig. 10a–i, the effective yield stress $\bar{\sigma}_y = \bar{\sigma}_e\left(\bar{\varepsilon}^{pl}_e\right)$ is presented as a function of the tungsten volume fraction f_W. The first line of subfigures is related to the technological yield limit at 0.2% effective plastic strain whereas the second and the third lines are related to later points on the yield curves with 1% and 10% effective plastic strain. The different rows of subfigures are related to temperatures of $T = 20$ °C, 600 °C and 1200 °C, respectively.

The technological yield limit $R_{p0.2} = \bar{\sigma}_y\left(\bar{\varepsilon}^{pl}_e = 0.002\right)$ for all random microstructures is found to be less than the prediction by the rules of mixture with a noticeable scatter at all temperatures investigated. Again, this effect is caused by the local residual stresses which develop during the initial cooling and re-heating cycle. Due to this effect, involving restricted local plastic deformation, no mathematically rigorous yield limit for the composite materials exists, even though a rigorous yield limit is assumed for the mechanical response of the constituents. The strongest effects of the residual stresses are observed at ambient temperature. In this case, the technological yield limits may even be below the yield limit of the vanadium phase. With increasing macroscopic plastic deformation $\bar{\varepsilon}^{pl}_e$ the yield stresses approach the prediction by the rules of mixture, since the residual stresses are levelled out by the overall plastic straining of the material. Especially at higher temperatures (1200 °C) the tungsten volume phase quickly becomes the dominant parameter.

For the unidirectionally infinite (UD) fiber reinforced composite type, the yield stress is strongly anisotropic. At all temperatures and equivalent plastic strain levels, the yield stress is found close to the prediction by the rules of mixture, provided that the material is loaded within the fiber direction. For normal deformation perpendicular to the fiber direction, a much weaker response is obtained. The yield stress decreases further, if the composite is loaded in a shear mode. In this case, an effective material response close to the behaviour of pure vanadium is obtained, irrespectively of the shear plane. For the aligned short fiber composite, the effective material behaviour is found to be similar to the behaviour of the random microstructure composite. This is distinctively different to the physical properties studied in the previous sections, where the UD and aligned short fiber composites exhibit a similar behaviour.

4.5. Creep resistance

The thermal design window of the material is bounded at the upper end by the development of excessive creep deformation at high temperature. For plasma facing components, an excellent creep resistance at considerable load levels is mandatory for temperatures up to $T = 1200$ °C. In order to study the effective creep response of the different composite design options, finite element analyses at $T = 900$ °C are performed, where the representative volume elements are subjected to constant uniaxial normal or shear stresses $\bar{\sigma}_{ij}$ after completing the initial thermal loading cycle. The applied stress level is chosen such that an effective v.Mises equivalent stress level of either $\bar{\sigma}_e = 120$ MPa or 200 MPa is reached. In the case of the lower load level, no significant rate-independent plastic deformation is possible whereas in the latter case, both creep and classical rate-independent plastic deformation might develop. The creep strain rates are computed for three different instants of time after one hour of loading, at $t = 10$ h

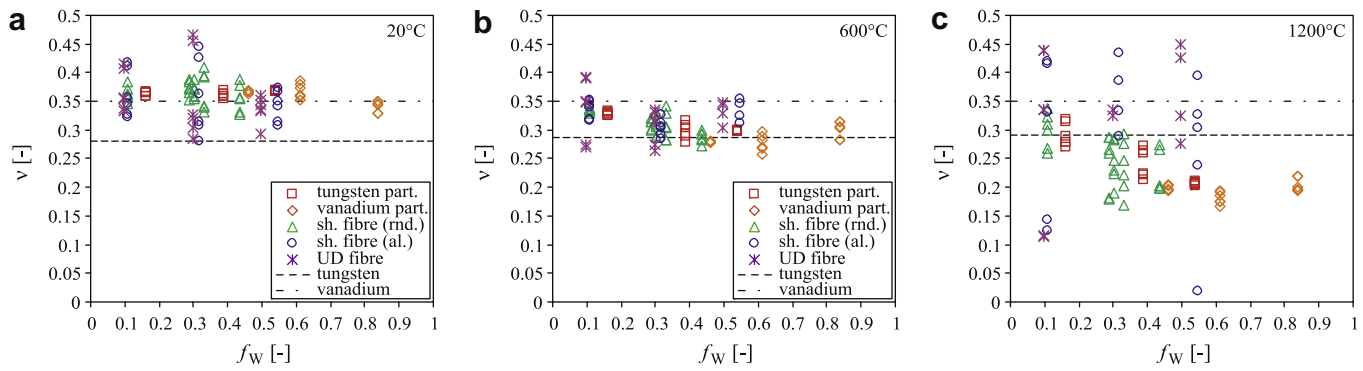

Fig. 9. Effective Poisson's ratio at different temperatures.

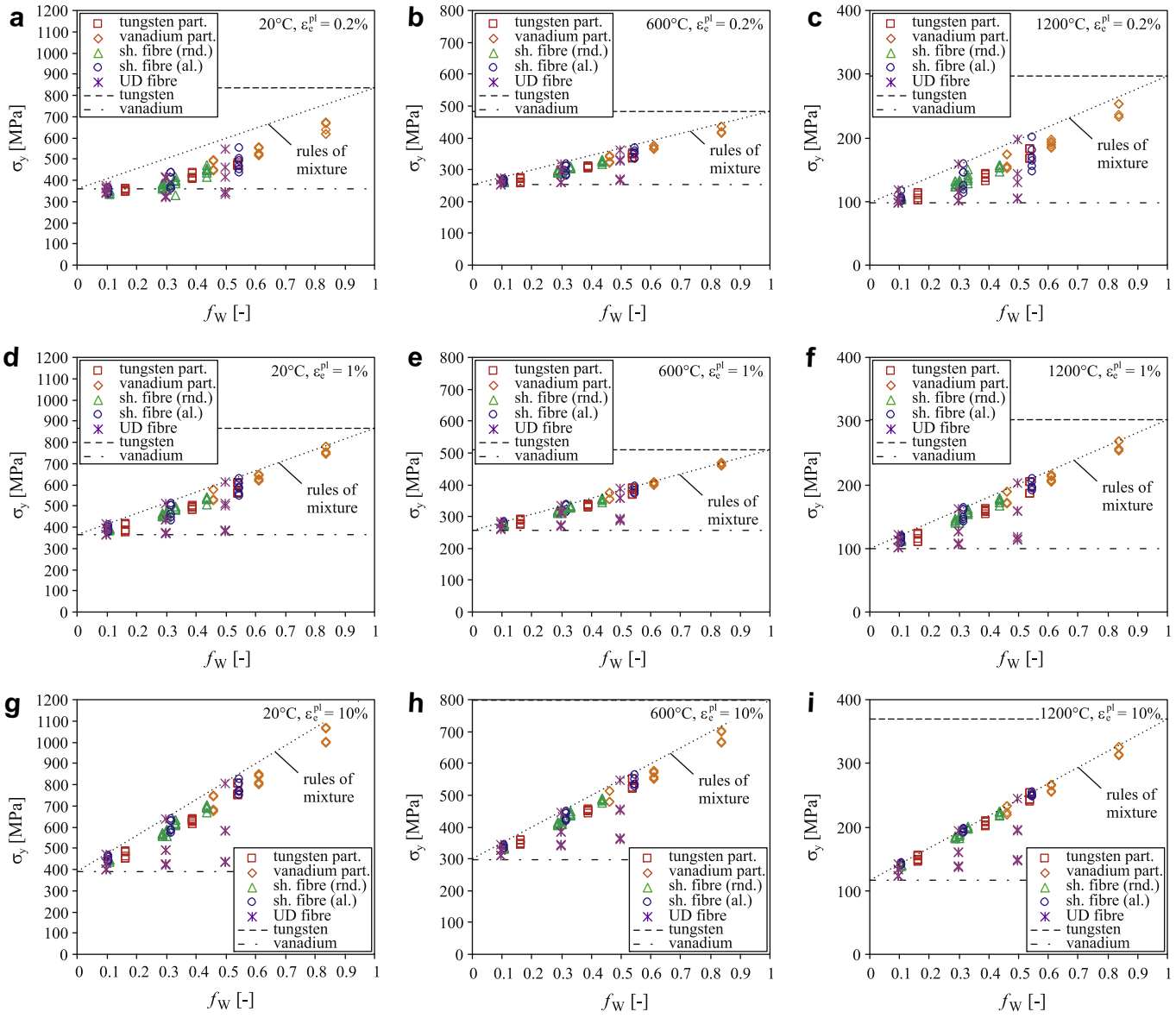

Fig. 10. Effective yield stress for different levels of equivalent plastic strain at different temperatures.

and at 100 h. The results for the two load levels and the three loading times are presented in Fig. 11a–f.

For the lower load level $\bar{\sigma}_e = 120$ MPa, a large scatter of creep rates is observed after 1 h of loading in Fig. 11a. In many cases, the creep rates exceed the corresponding creep rate for pure vanadium. This effect is caused by the internal residual stresses due to the thermal mismatch of the two constituents. The corresponding residual elastic strain energy acts as an additional driving force for the creep deformation until its release during the initial stage of creep deformation. With increasing time of stress exposure and thus increasing creep deformation, the additional driving force vanishes, resulting in decreasing creep rates. After 100 h of loading time, creep effects for tungsten volume fractions of $f_W = 0.4$ and beyond become insignificant compared to the creep of pure vanadium.

At the higher load level $\bar{\sigma}_e = 200$ MPa, a less distinct scatter of the results is observed even for short loading times of $t = 1$ h, Fig. 11d. The higher stress level causes higher creep rates and thus a faster release of the residual stresses caused by the thermal mismatch and the related residual strain energy. Nevertheless, even for the larger load level, where the initial residual strain energy is released quickly, decreasing creep rates are observed with increasing loading time. This effect is caused by an internal redistribution of the stresses from deviatoric stress states which are relaxed due to plastic and creep deformation towards hydrostatic stress states which cannot be relaxed by volume preserving plastic or creep deformation. This stress redistribution is caused by the restricted creep deformation of the tungsten inclusions at $T = 900$ °C which constrains the deviatoric deformation of the otherwise heavily creeping vanadium matrix. With increasing creep deformation, these deformation constraints increase resulting in decreasing effective creep rates. At higher effective load levels or larger creep times, these deformation constraints become the dominant mechanisms to restrict the creep deformation of the weak vanadium matrix, resulting in small creep rates of the composite even for moderate tungsten volume fractions.

4.6. Fracture toughness enhancement

The fracture toughness enhancement of brittle materials with ductile reinforcements can be estimated by means of a Dugdale–Barenblatt [2,7] type cohesive zone model. The basic idea of this

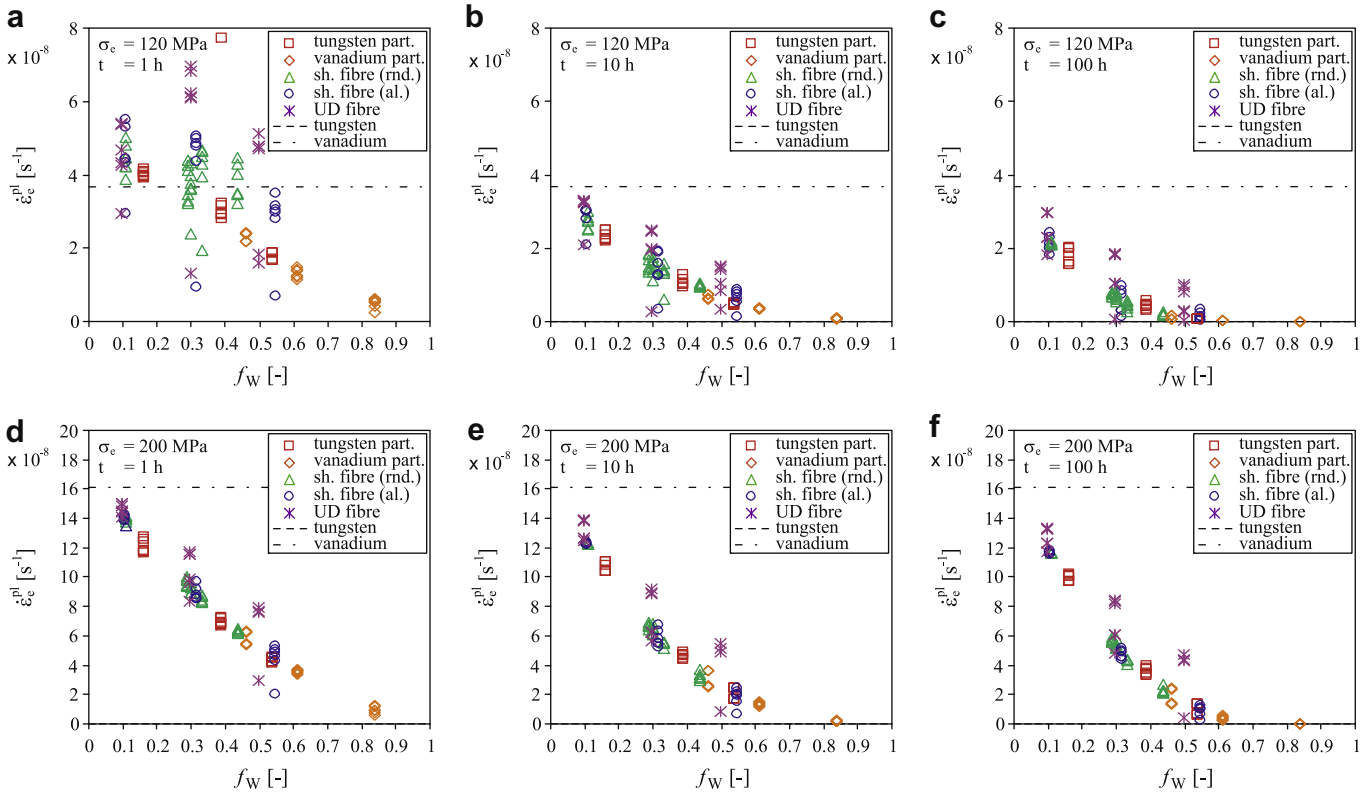

Fig. 11. Effective creep rates at $T = 900\,^{\circ}C$ for different load levels at different instants of time.

approach is the assumption that the separation of the material during crack propagation is a degrading process rather than an instantaneous event (e.g. [22]). The brittle phase is assumed to fail first while the ductile phase forms crack bridges which partially shield the crack front from the externally applied load K_I^{appl}. With increasing crack opening displacement COD, the ductile crack bridges fail in a ductile mode. The ductile dissipation during this degrading process extends the overall energy release rate of the composite material. Mathematically, the degrading process is modeled by a virtual extension of the physical crack by a cohesive zone. Within the cohesive zone, the ductile separation process is modeled by application of cohesive tractions $\sigma^{coh}(COD)$ on the crack faces tending to close the crack.

The cohesive law $\sigma^{coh}(COD)$ for the different composite types can be estimated from finite element analyses. For this purpose, the finite element models employed in the previous investigations are re-formulated by removing the periodic boundary conditions for the brittle phase on the surface perpendicular to the external loading direction. Hence, the brittle phase on the respective boundary is assumed to be broken whereas the ductile phase remains intact and thus bridges the crack along the respective surface of the representative volume element. Subsequently, the representative volume element is deformed by a prescribed effective strain $\bar{\varepsilon}_{(ii)}$ normal to the direction of the crack plane. The analysis is performed for crack orientations in all three spatial directions in order to gain some statistical information regarding the effect of the microstructural disorder.

From the results of the finite element analyses, the cohesive dissipation W^{coh}, the cohesive stress σ^{coh} and the (virtual) crack opening displacement COD can be determined in a straight forward manner as the total dissipated plastic work W^{pl}, the resulting effective stress $\bar{\sigma}_{ij}$ within the loading direction and the corresponding extension $\bar{\varepsilon}_{ij} l_i$ of the representative volume element. In this context, the cohesive zone covers the tearing work as well as the energy dissipated in the direct vicinity of the crack bridging zones which is assumed to be associated directly with the failure process. For these investigations, an edge length l^{RVE} of $l_i = 0.1$ mm is assumed for the representative volume element. Ductile failure of

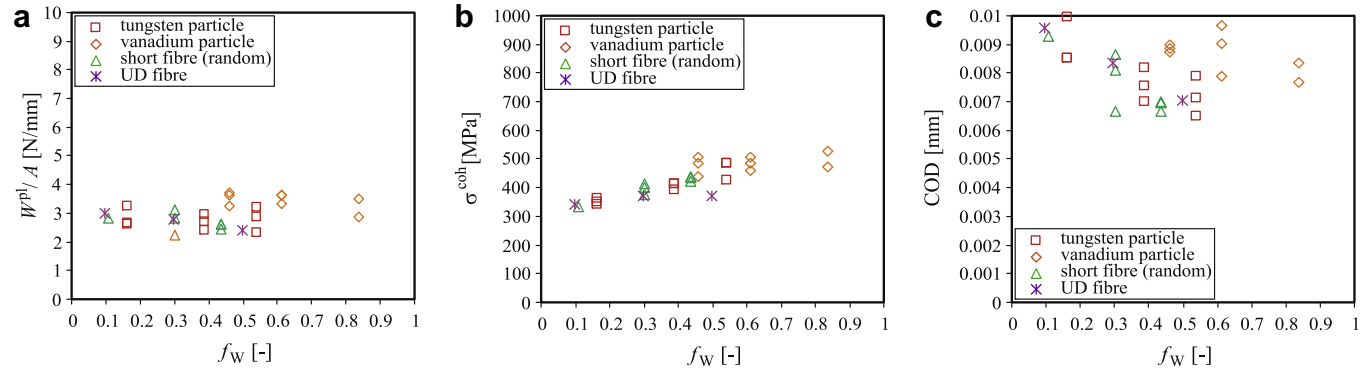

Fig. 12. Cohesive properties at $T = 300\,^{\circ}C$.

the crack bridging phase is assumed, if the average of the accumulated equivalent plastic strain $\bar{\varepsilon}_e^{pl}$ in the cracked surface reaches a critical value, assumed to be 0.1.

Although the computed cohesive parameters provide only rough estimates due to the lack of a reliable micromechanical ductile failure strength and due to the fact that in addition to the accumulated plastic strain, the ductile failure is strongly affected by the local stress triaxiality, the results can well be used for a comparison of the toughness potential of the different composite types. The results for the critical cohesive energy density W^{pl}/A, the critical cohesive stress σ^{coh} and the critical crack opening displacement COD at a temperature of $T = 300\,^{\circ}C$ are presented in Fig. 12. Since plasticity is not localized and crack propagation is not realistically considered, these results may be regarded as an upper limit of possible toughening.

Surprisingly, the cohesive energy dissipation W^{pl} and thus the possible fracture toughness enhancement are similar for all composite types. The tungsten volume fraction f_W is found to have only minor effects on the possible toughness enhancement what means that all composite types have the potential to essentially increase the fracture toughness of tungsten-based materials. Nevertheless, increasing tungsten volume fractions cause increasing cohesive stresses σ^{coh} at decreasing critical crack opening displacements COD what results in smaller cohesive zones with higher dissipation densities.

5. Preliminary experimental investigation

5.1. Material

For a preliminary experimental investigation of the potential of the proposed tungsten–vanadium composite, a first trial heat of the material has been produced and tested for its fracture toughness at low temperature and its creep resistance at high temperature. The material was processed by a powder metallurgical route using a hot isostatic pressing technique. For this purpose, tungsten and vanadium powders were mixed with a tungsten volume fraction of $f_W = 50\%$. The material was sintered for one hour at a temperature of 1500 °C under a pressure of 30 MPa. Subsequently, the material was cooled down to ambient temperature at a rate of 10 K/min with possibly lower rates below 600 °C. A total of six plates with the outer dimensions of 5 mm × 14 mm × 87 mm as well six plates with 5 mm × 10 mm × 45 mm were manufactured. From the plates, tensile and fracture mechanics specimens were prepared.

A metallographic investigation reveals that the material is of the particle composite type with distinct clusters of embedded pores as it can be observed in Fig. 13a and b. The pore density is varying spatially. The chemical contents of the different material areas visible in the section presented in Fig. 13 were investigated in more detail using energy dispersive X-ray microanalysis. The results are presented in Fig. 13c and d, where the light areas indicate a high content of more heavy atoms whereas the medium to dark areas indicate a larger percentage of less heavy atoms. For the points marked in Fig. 13d, a detailed analysis was performed, revealing that the microstructure of the material consists of pure tungsten particles, surrounded by an interphase consisting of a solid solution of tungsten and vanadium with a tungsten volume fraction of approximately $f_W = 68\%$. The inclusions and the surrounding interphases are embedded into a solid solution of both metals with a much lower tungsten content of approximately $f_W = 14\%$. The solid solutions have developed due to diffusion processes during the processing of the material. The diameter of the inclusions and the surrounding interphases was found to be approximately 50 μm.

5.2. Creep resistance

For an investigation of the upper limit of the thermal design window of the material, tensile creep experiments at high

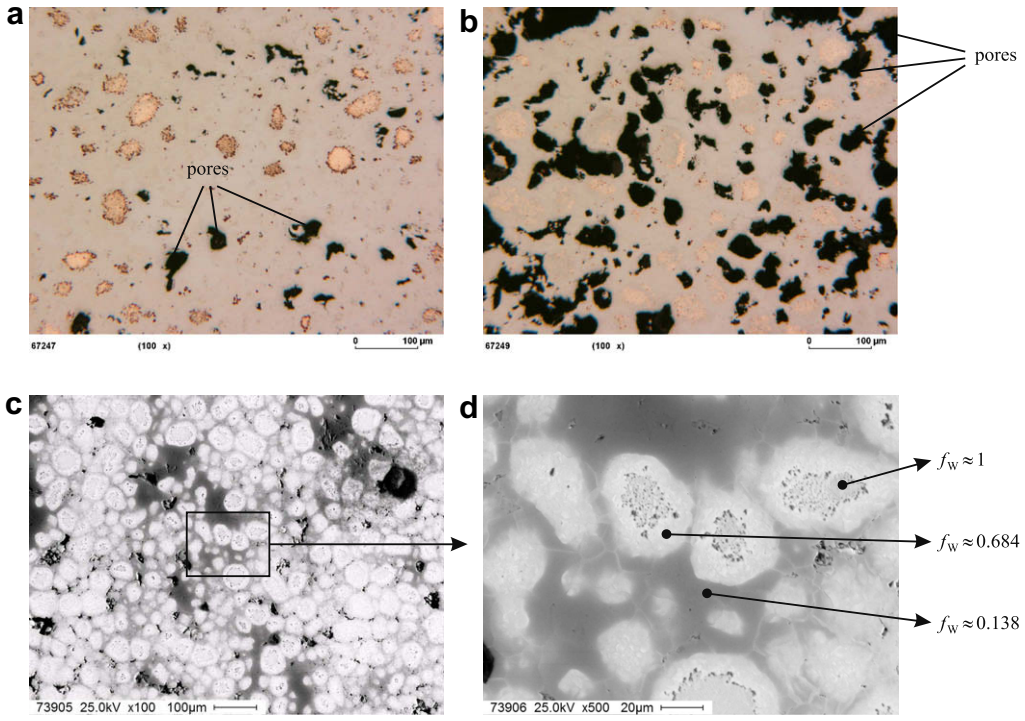

Fig. 13. Metallographic analysis of the trial heat: (a) section taken from the specimen center, (b) section taken close to the specimen surface, (c) section taken from the specimen center (SEM), (d) detail.

temperatures were performed. From larger plates, tensile specimens with rectangular cross section and 24 mm nominal gauge length were cut by electrical discharge machining. The specimens were tested under load control in an Instron 8562 testing machine using a ceramic loading device. Due to severe oxidation of the material at higher temperatures, the tests were performed in a nitrogen environment. Therefore, the specimens and the loading device were encapsulated in a nitrogen-filled pipe. The entire experimental assembly was heated from the outside to the desired temperature. It has to be mentioned that the choice of a nitrogen environment can result in a strengthening of the material. On the other hand, the formation of microcracks in a brittle nitride surface layer might result in a weakening of the material. Therefore, care has to be taken when evaluation the results.

The creep experiments were performed at constant nominal stress levels with $\sigma_{appl} = 20$ MPa, 40 MPa, 60 MPa, 80 MPa and 100 MPa, respectively. A test temperature of $T = 1000\,^{\circ}C$ was applied in all creep tests. During the tests, the applied force and the cross-head displacement were recorded. Due to the encapsulation of the experimental setup, no direct extensometer measurement of the displacements within the gauge section of the specimens was possible. Therefore, the creep strain rate $\dot{\varepsilon}_e^{pl}$ in the gauge section had to be estimated from the cross-head displacement rate $\dot{u}_{ch}$ in conjunction with a finite element simulation of the test calibrated by post test elongation measurements.

The results for the cross-head displacement rate $\dot{u}_{ch}$ and the estimated creep strain rate $\dot{\varepsilon}_e^{pl}$ are presented in Fig. 14a and b. Secondary creep with constant velocity is observed for the lower load levels with a nominal stress of $\sigma_{appl} = 20$ MPa and 40 MPa as well as towards the end of the creep test performed with $\sigma_{appl} = 80$ MPa. For the tests performed with $\sigma_{appl} = 60$ MPa and $\sigma_{appl} = 100$ MPa no secondary creep range has developed prior to rupture of the specimens. Decreasing slopes of the displacement–time curves observed in the initial range of the load history indicate the development of an increasing creep constraint during this range in the time scale as predicted by the numerical simulations (see Section 4.5). Despite some scatter, the logarithm of the secondary creep rate depends linearly on the applied load as known from most other materials. Compared to the creep rates obtained by Wheeler et al. [28] for pure vanadium tested at $T = 1000\,^{\circ}C$, distinct advantages of the present material are observed. In the load range from $\sigma_{appl} = 20$ MPa to 40 MPa, the creep rate of the present tungsten–vanadium composite is reduced to approximately 0.2% of the creep rate expected for pure vanadium. For higher load levels, no experimental data are available for comparison due to the excessive creep deformation of pure vanadium in this load range at temperatures of 1000 °C and beyond. Further advantages of the composite material could be expected for improved heats with lower porosity.

5.3. Fracture toughness

For the investigation of the lower limit of the thermal design window of the proposed composite material, pre-cracked three point bend bars were machined. The dimensions of the specimens coincided with the standard SE(B) 5×10 geometry according to ASTM Standard E 1921 [1] with a 3 mm-deep fatigue-crack starter notch. In order to avoid any possible mechanical damage of the material due to the preparation, the fatigue crack starter notches were cut by electrical discharge machining. Subsequently, the specimens were fatigue pre-cracked in a RUMUL electro-mechanical resonance machine at the lowest possible load level of approximately 4 $MPam^{1/2}$. In order to avoid accidental failure during the specimen preparation, fatigue pre-cracking was discontinued in most cases immediately after sharp cracks were first visible on both sides of the specimens, resulting in crack length ratios in the range from $a/W = 0.4$ up to $a/W = 0.79$. The specimens were tested under displacement control in a Schenck EB 50 testing machine at the lowest possible cross-head speed of 0.001 mm/s. All tests were performed at ambient temperature.

The recorded load vs. load-line displacement curves reveal that the specimen failed after some amount of overall plastic deformation. The fracture toughness results are found in the range from $K_{Jc} = 9.0$ $MPam^{1/2}$ to 14.8 $MPam^{1/2}$ with an average fracture toughness of 11.8 $MPam^{1/2}$ as shown in Fig. 15a. A fractographic investigation of the fracture surfaces using scanning electron microscopy reveals that transgranular (quasi-) cleavage was the dominant failure mechanism. Nevertheless, some ranges of intercrystalline fracture can also be detected in Fig. 15b. In areas with high void volume fraction, a significant amount of the fracture surfaces is formed by voids and non-bonded areas.

Compared to fracture toughness results reported in the literature, the present values at a first glance provide only minor or vanishing improvements. The fracture toughness for tungsten single crystals at ambient temperature has been determined by Gumbsch et al. [11] and Riedle et al. [21] to be between 6 $MPam^{1/2}$ and 20.2 $MPam^{1/2}$, strongly depending on the orientation of the crack plane within the crystal lattice. For polycrystalline tungsten, fracture toughnesses in the range of 13—15 $MPam^{1/2}$ with a slight enhancement for tungsten–rhenium alloys have been reported by Mutoh et al. [18]. In a recent study, Rupp et al. [23] found the fracture toughness for pure tungsten between 13 $MPam^{1/2}$ normal to rolling direction and 8 $MPam^{1/2}$ for all other directions. In this study, a general decrease in the fracture toughness with decreasing grain size was observed, partially caused by the formation of a damage zone consisting of intergranular cracks ahead of the crack front. A similar grain size effect has also been reported in a recent contribution by Faleschini et al. [9]. Since the grain size of the present material is smaller than in their study and especially due to the

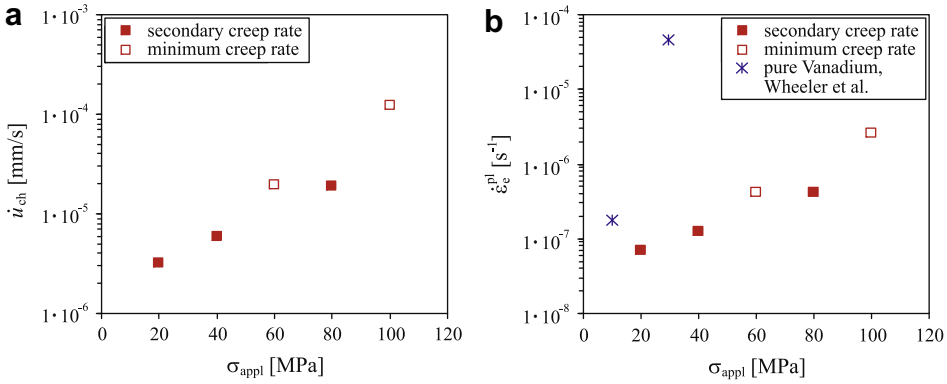

Fig. 14. Experimentally determined creep rates at $T = 1000\,^{\circ}C$.

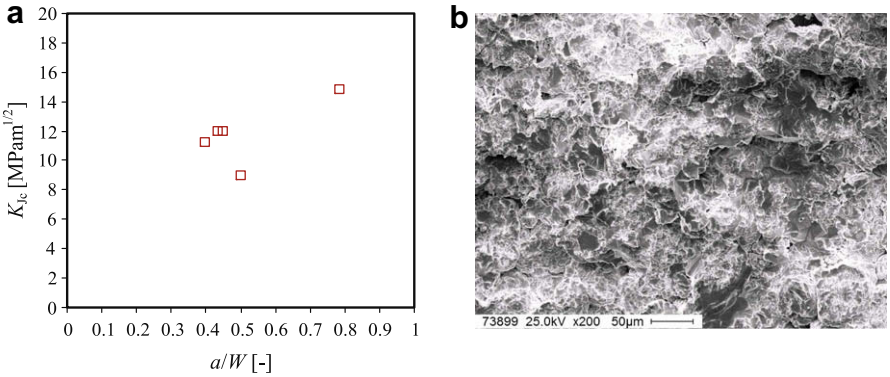

Fig. 15. Experimentally determined fracture toughness and fracture surface.

large void volume fraction of the present material, a much lower fracture toughness would have to be expected for pure tungsten specimens manufactured by a similar powder metallurgical route and with a similar void volume fraction as for the present material. Therefore, and due to the failure of the specimen after a slight to moderate overall plastification, the fracture results reveal that there is a definite potential for a fracture toughness enhancement by the presence of the vanadium phase. Nevertheless, the microstructure of the trial heat of the proposed material tested in the present study is still sub-optimal.

6. Conclusions

The objective of the present study is an exploration of the potential of tungsten–vanadium composites for high temperature application with a wide-range thermal operation window. In a first approach, the potential of different microstructural design options, including particle reinforced composites with both tungsten and vanadium matrix, random and aligned short fiber reinforced composites as well as infinite unidirectionally tungsten fiber reinforced composites has been studied numerically. In a second approach, a trial heat of the material has been processed and tested for its creep resistance at 1000 °C as well as its fracture toughness at ambient temperature.

A comparison of the numerical results for the effective thermomechanical material properties of the different microstructural design options shows that the tungsten volume fraction is the most important parameter. For primarily uniaxial loading, advantageous material properties can be obtained by the use of unidirectionally tungsten fiber reinforced composites, provided that the fiber direction is chosen in an appropriate manner for the specific load case under consideration.

Although the tungsten volume fraction is found to be the most important parameter for all composite type, the simple rules of mixture provide only rough estimates on the effective properties. Internal deformation constraints caused by the mismatch in the thermal expansion properties of the matrix and the inclusions in conjunction with the severe temperature changes between processing temperature, ambient temperature and the service temperature result in distinct internal deformation and, since the deformation is constrained, in distinct residual stresses. These residual stresses have a strong impact on the effective properties and for repeated thermal cycling may also affect the thermomechanical fatigue properties of the material.

With respect to a possible extension of the thermal operation window compared to the operation windows of pure tungsten and pure vanadium, the results reveal a distinct enhancement of the creep resistance of vanadium by tungsten reinforcements. The creep resistance increases during the first stage of creep deformation due to a transition of deviatoric (v. Mises-) stresses towards hydrostatic stresses. By means of this mechanism, an increased creep resistance develops even for moderate to medium tungsten volume fractions. A rough estimation of the possible fracture toughness enhancement at lower temperatures reveals the existence of a potential for toughness enhancement. Nevertheless, a quantification of the potential is difficult due to the lack of a reliable micromechanical (ductile) failure criterion for the vanadium phase.

The experimental investigation of a trial heat of the proposed composite material shows a distinct enhancement of the creep resistance compared to results for pure vanadium reported in the literature. As predicted, the creep resistance increases with increasing creep deformation during the initial loading stage. Fracture mechanics tests at ambient temperature reveal a failure of the specimen after some overall plastic deformation. Compared to results reported in the literature, the fracture toughness is only slightly increased. Nevertheless, since the trial heat of the composite material had a clearly sub-optimal microstructure with a high amount of pores and nonbonded zones and due to the possibly more severe test conditions in the present study, these – though sub-optimal – results clearly reveal the potential of the proposed composite towards an enhancement of the lower thermal design limit of tungsten provided that the microstructure of the material can be improved. Possible improvements may be achieved by application of rapid sintering techniques or a processing of the material at lower temperatures.

Acknowledgement

This work, supported by the European Communities under the contract of association between EURATOM and Forschungszentrum Karlsruhe, was carried out within the framework of the European Fusion Development Agreement. The views and opinions expressed herein do not necessarily reflect those of the European Commission. The financial support is gratefully acknowledged.

References

[1] ASTM Standard E 1921-05, Standard Test Method for Determination of the Reference Temperature, T_0, for Ferritic Steels in the Transition Range, ASTM International, West Conshohocken, PA, 2005.
[2] G.I. Barenblatt, J. Appl. Math. Mech. 23 (1959) 622–636.
[3] J.F.W. Bishop, R. Hill, Philos. Mag. 42 (1951) 414–427.
[4] V.A. Borisenko, V.V. Bukhanovskij, I. Mamuzic, Strength Mater. 37 (2005) 584–592.
[5] E.A. Brandes, G.B. Brook (Eds.), Smithells Metals Reference Book, Butterworth Heinemann, Oxford, 1998.
[6] E.G. Donahue, G.R. Odette, G.E. Lucas, J. Nucl. Mat. 283–287 (2000) 637–641.
[7] D.S. Dugdale, J. Mech. Phys. Solids 8 (1960) 100–104.

[8] T. Dümmer, J.C. Lasalvia, G. Ravichandran, M.A. Meyers, Acta Mater. 46 (1998) 6267–6290.
[9] M. Faleschini, H. Kreuzer, D. Kiener, R. Pippan, J. Nucl. Mater. 367–370 (2007) 800–805.
[10] P. Gumbsch, J. Nucl. Mater. 323 (2003) 304–312.
[11] P. Gumbsch, J. Riedle, A. Hartmaier, H.F. Fischmeister, Science 282 (1998) 1293–1295.
[12] R. Hill, Proc. Roy. Soc. A 65 (1952) 349–354.
[13] J. Hohe, W. Becker, Compos. B 32 (2001) 185–197.
[14] J. Hohe, W. Becker, Int. J. Mech. Sci. 45 (2003) 891–913.
[15] R.J. Kurtz, K. Abe, V.M. Chernov, V.A. Kazankov, G.E. Lucas, H. Matsui, T. Muroga, G.R. Odette, D.L. Smith, S.J. Zinkle, J. Nucl. Mater. 283–287 (2000) 70–78.
[16] M. Li, T. Nagasaka, D.T. Hoelzer, M.L. Grossbeck, S.J. Zinkle, T. Muroga, K. Fukumoto, H. Matsui, M. Narui, J. Nucl. Mater. 367–370 (2007) 788–793.
[17] R.W. Margevicius, J. Riedle, P. Gumbsch, Mater. Sci. Eng. A 270 (1999) 197–209.
[18] Y. Mutoh, K. Ichikawa, K. Nagata, M. Takeuchi, J. Mater. Sci. 30 (1995) 770–775.
[19] R.G. O'Donnell, R.L. Woodward, Metall. Trans. 21a (1990) 744–748.
[20] E. Pink, S. Kumar, R. Grill, Int. J. Refrac. Met. Hard Meter. 15 (1997) 301–309.
[21] J. Riedle, P. Gumbsch, H.F. Fischmeister, Phys. Rev. Let. 76 (1996) 3594–3597.
[22] A.A. Rubinstein, K. Xu, J. Mech. Phys. Solids 40 (1992) 105–125.
[23] Rupp, D., Zeng, X., Weygand, S.M., Hartmaier, A., Loading rate dependence of the fracture toughness of polycrystalline tungsten: experiments and modelling, in: Proc. 17th Eur. Conf. Fracture, Brno, September 02–05, 2008, pp. 667-674.
[24] W. Schreiter, Seltene Metalle Band III, VEB Deutscher Verlag für Grundstoffindustrie, Leipzig 1962 (in German).
[25] A.A.F. Tavassoli, J. Nucl. Mater. 302 (2002) 73–88.
[26] M. Vill, P.D. Adams, S.M. Yalisove, J.C. Bilello, Acta Metall. Mater. 43 (1995) 427–437.
[27] Wahrenberg, R., Untersuchung der elektrischen Struktur flüssiger Metalle mittels zeitaufgelöster Photoelektronenmikroskopie, PhD-Thesis, University of Basel, 2001 (in German).
[28] K.R. Wheeler, E.R. Gilbert, F.L. Yaggee, S.A. Duran, Acta Metall. 19 (1971) 21–26.
[29] S.J. Zinkle, N.M. Ghoniem, Fusion Eng. Des. 51–52 (2000) 55–71.